Insight into martian crater degradation history based on crater depth and diameter statistics

Sylvain Breton, Cathy Quantin-Nataf, Lu Pan, Lucia Mandon, Matthieu Volat

Insight into Martian crater degradation history based on crater depth and diameter statistics

Sylvain Breton[1], Cathy Quantin-Nataf[2], Lu Pan[3], Lucia Mandon[2], Matthieu Volat[2]

1: Université de Loraine, CRPG, 2: Université de Lyon, 3: University of Copenhagen

1. Introduction

Planetary landscapes are shaped by a wide range of geologic processes leading to diverse morphologies. Among those processes, impact cratering is observed from asteroids to planets' surfaces. The bowl-shaped cavities formed by hypervelocity impacts are easy to observe from orbit at a planetary scale, and are therefore studied since the 1940s (Young, 1940). Despite their ubiquity, crater densities and shapes are significantly different from a surface to another, even on the same body.

As the exposure duration to impact bombardment of the surface increases, the number of craters on the surface increases. In other words, the number of craters on a surface, represented as Crater Size Frequency Distributions (CSFD), is proportional to its age. Crater density was first used to date surfaces in a relative sense (Baldwin, 1949). Later, returned samples from the Apollo and Luna missions provided absolute ages for Lunar surfaces (Shoemaker, 1970; Stöffler and Ryder, 2001), allowing the calibration a model that links the absolute age to the crater density of a surface (Hartmann, 1970; Neukum et al., 1977). This field of research yielded a dating method that is now widely used on many bodies of the solar system (Daubar et al., 2013; Ivanov, 2001; Neukum et al., 2001).

Shape of craters depends on both initial crater shape and later modification by geologic processes. The initial shape of a crater mainly depends on impactor size, target properties (Melosh, 1989; Schenk et al., 2021) and impact velocity and angle (Daubar et al., 2014; Plescia and Cintala, 2012). Despite this variability, fresh crater shape can be estimated for a given diameter, especially when considering an homogenous geological unit with consistent surface properties (Garvin and Frawley, 1998; Pike, 1974; Robbins and Hynek, 2012a). Crater shapes are thereafter modified by surface processes of various kinds and intensities. As an example, the absence of rim can be interpreted by a strong erosion (Mangold et al., 2012; Neukum et

al., 2001) and a flat crater floor often indicates infilling with sediments or lava flows (Craddock et al., 1997).

The last stage of crater modification is the total disappearance of the crater. Since small craters are degraded faster than big ones, this phenomenon creates complications when using crater densities to date planetary surfaces. This lack of small craters, called the Opik effect (Opik, 1966), has first been observed on Mars, where the density of craters smaller than 20 km of diameter is lower than the density predicted by the isochrons determined from bigger craters. This observation is one of the many evidences that Mars surface witnessed surface modification processes which were more intense than the ones observed today (Opik, 1966)

Measuring intensity, age and duration of resurfacing events remains challenging (Michael, 2013), as information on previous events is lost alongside erased craters. Including crater obliteration in the cratering models provide a better understanding of crater population and surface processes that affected them (Pan et al., 2019; Quantin-Nataf et al., 2019). However, those models remain under-constrained, and requires additional assumptions on geological processes involved to explain the observed CSFD. Moreover, in those models, the shape of fresh craters is considered known and independent from the target properties. In these cases, scaling models deduced from global crater statistics are used to set their initial crater shape, ignoring target properties effect on the initial crater shape which is not well known especially for craters smaller than 1 km (Barlow, 2005; Pike, 1980).

Adding systematic crater morphometric measurements can provide better understanding of crater populations evolution beyond what CSFDs can provide. Studying crater obliteration using a dataset of crater diameter and depth was first proposed by Carr (1992). With the recent improvement of mathematical tools, data and computer power, it is now possible to develop the idea, providing a continuous and global picture of Martian crater obliteration. Here, we propose the introduction of a new representation of crater population that provides information on the degradation state of the craters. By analogy with CSFD, we produced Crater Size and Depth Frequency Distribution (CSDFD) along with the tools to interpret this representation in terms of crater obliteration. This type of analysis is especially useful for interpreting Martian landscapes as crater populations are often modified. We also highlight at the end new insights into Mars geologic history by applying our method to a Martian crater database (Robbins et al., 2012ab).

2. Method

In this section, we describe in detail the methodology to analyze crater size and depth distribution developed in this study. We first introduce the crater size and depth frequency distribution (CSDFD). Then we describe the forward modelling approach to estimate the varying obliteration rate with time from the built-in CSDFD. In the end, we discuss the Martian crater database used to apply our approach.

2.1 Building CSDFD

To account for the increased number of small craters, frequencies of craters relative to their diameter, or crater size frequency distribution (CSFD) (Young, 1940), are generated based on an exhaustive catalogue of craters observed on the surface.

This representation is originally a histogram of crater density plotted against different crater size bins. In this study, we used differential CSFDs as they are more sensitive to slope variation of the crater size distribution such as the ones due to the Opik effect (Hartmann, 2005). Hereafter, CSFD only refers to differential CSFD. For a given diameter bin *j*, the crater density is calculated as:

$\mathrm{CSFD}_j = \frac{N_j}{Area \times \delta D_j}$, with N_j the number of craters in the bin, $Area$ the studied area in km^2 and δD_j the width of the diameter bin in km.

Recently, Robbins et al. (2018a) presented a new approach to build CSFD using kernel estimator and estimated error using a method of bootstrapping. This approach presents many advantages such as offering a continuous representation of the CSFD or the inclusion of the error on measured diameters.

The kernel estimator aims to find the frequency distribution (the CSFD) that produces an observed dataset of crater diameter $\mathbb{D} = \{D_1, D_2, \dots, D_n\}$. The kernel density estimator can be described as the sum of the observed data, convoluted with a kernel function K with a bandwidth h (equation 1).

$$\widehat{CSFD}_h(D) = \frac{1}{n \times h} \sum_{i=0}^{n} K\left(\frac{D - D_i}{h}\right) \qquad (1)$$

In our case the dataset is now composed of 2 parameters, each crater C_i is defined by its diameter and depth. Since the crater density has a power-law relationship with the diameter, we used the logarithm of diameter $C_i = (\log(D_i), d_i)^T$. The whole set of craters is denoted $\mathbb{C} = \{C_1, C_2, \dots, C_n\}$. In this case, the kernel function used is a bivariate distribution, function of depth and diameter. The kernel function choice does not change much the produced density (Robbins et al., 2018a). We used a multivariate normal kernel function. The CSDFD is then computed as:

$$\begin{cases} \widehat{CSDFD}_H(D,d) = \dfrac{1}{n}\displaystyle\sum_{i=0}^{n} K_H(C - C_i) \\ K_H(c) = \dfrac{1}{2\pi}\, H^{-1/2} \times \exp\left(\dfrac{1}{2} c^T H^{-1} c\right) \end{cases} \quad (2)$$

In the 2D case, the bandwidth h has been replaced by a 2×2 bandwidth matrix H. The choice of the bandwidth is more critical than the used kernel function (Robbins et al., 2018a; Scott, 2012). This is also true for the choice of H. Not only H affects how much the kernel spreads, but it can also rotate and modify its ellipticity.

We used a rule of thumb (Scott, 2012) to compute the bandwidth matrix H (e.g. the width, aspect ratio and rotation of the kernel function) and the final kernel density. This process was performed using a Gaussian kernel function (the built-in Python function, gaussian_kde from scipy stats). Like the CSFD, the density of crater is normalized by the diameter step δD and the depth step δd. Hence, the produced densities are expressed in km^{-4} (equation 3):

$$CSDFD_{i,j} = \frac{\widehat{CSDFD}_h(D_i,\, d_j)}{Area \times \delta D_i \times \delta d_j} \quad (3)$$

In our analysis, starting from the new formalism proposed by Robbins et al. (2018a), we implemented a kernel density estimator to produce a continuous representation of the diameter and depths of a crater population. This representation, called CSDFD contains information not only on the number of craters, but also on their diameter and depth.

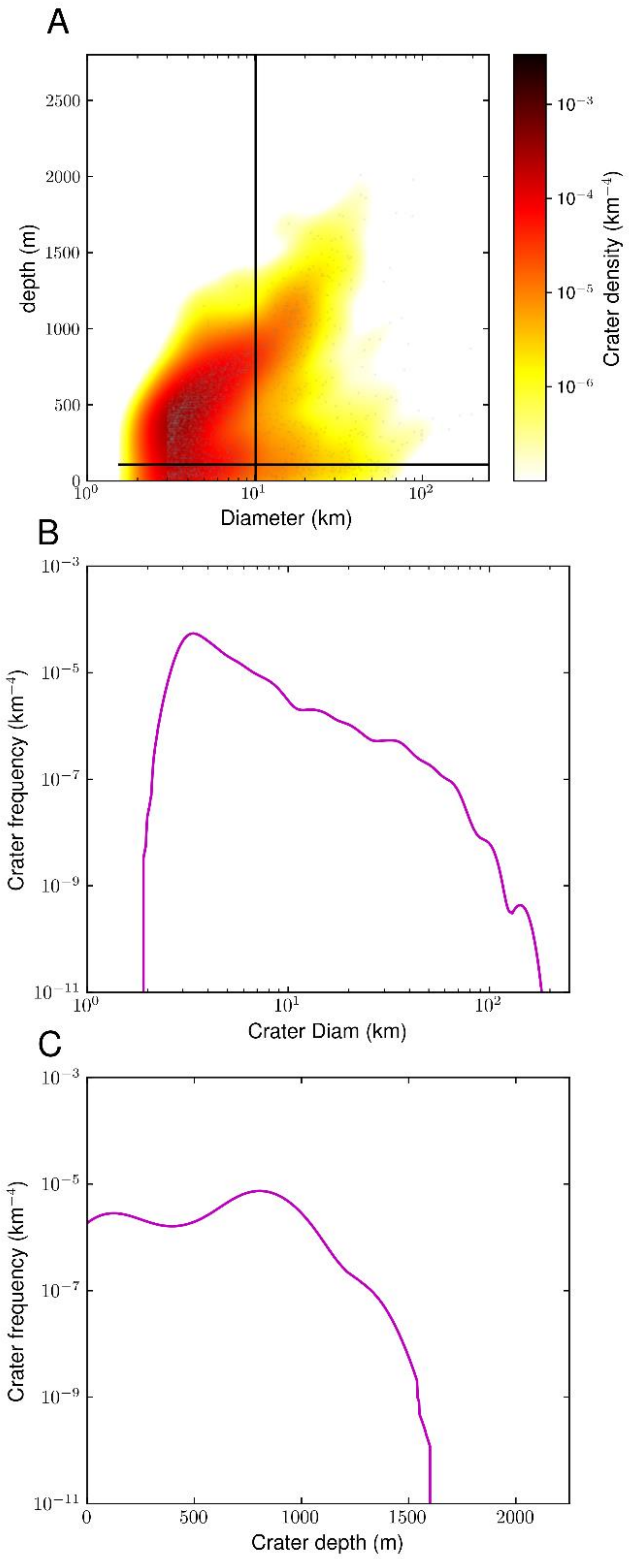

Figure 1: Example of a Crater Size and Depth Frequency Distribution computed from 57 333 craters present on the Martian Noachian Highlands (Robbins and Hynek, 2012b). *A The crater frequency is represented by the colormap, each crater used to compute the CSDFD is represented as a grey dot. Black lines indicate the diameter and depth cross-section represented in B and C.*

2.2 Deriving crater obliteration rates from CSDFD

CSDFDs are a representation of a crater population that includes information on the degradation state of a crater population. We build this representation using new statistical methods. However, note that CSDFD can also be built faster and more easily using a 2D histogram of depth and diameter. We propose here a method to interpret CSDFD in terms of crater obliteration rates.

To interpret CSDFD, we used a cratering model and an obliteration model. No model of the initial shape of crater is needed as the deepest observed craters are directly considered to be the freshest.

As mentioned earlier, the density of craters depends on the age of the surface, T, and the diameter, D. Equation 4 describes this model (Hartmann and Neukum, 2001; Neukum et al., 2001).

$$\begin{cases} \log\left(F_{crat}(D,T)\right) = \log\left(F_{crat,\,1\,km,\,T}\right) \times \sum_{k=1}^{m} a_k \times \log\,(D)^k \\ F_{crat,1\,km}(T) = C_1 \times (e^{T \times C_2} - 1) + C_3 \times T \end{cases} \quad (4)$$

With F_{crat} the cumulative density of craters (km^2), D the diameter (km) and T the age of the surface (Gy). The indexes a_k and C_l are specific to the studied body and the model used. We used the crater production function from Ivanov (2001) for Mars. The differential form of this equation is used to get the density of crater for a specific diameter and is denoted $f_{crat}(D,T) = \frac{\delta F(D,T)}{\delta D}$.

To mimic the condition where we have no prior knowledge about the specific geological processes operating, we used a very simplistic model in which craters are only degraded through a reduction of their depth at a rate *r* (equation 5).

$$D(T) = D_0 - r \times T \quad (5)$$

In this representation of the crater size-frequency, for a given diameter, the youngest craters are the deepest ones, and they evolve toward shallower depth without any change in diameter. To first order, the reduced crater depth is within expectation in all geological

processes that result in crater degradation. In most cases, the decrease of crater depth leads to an increase in the diameter, here, for computation stakes, this phenomenon is not considered. The effects of this assumption will be discussed in section 5.1.1.

For a given diameter bin, we can model the expected density according to age. An inverse cumulative crater depth frequency distribution $CDFD_i(d)$ is computed for every diameter bin i (equation 6) with $f_{crat}(D_i, age)$ computed thanks to equation 4.

$$\begin{cases} CDFD_i(d_j) = \sum_{u=j}^{N_j} \delta d_u \times CSDFD_{i,u} \\ CDFD_i(d_j) = f_{crat}(D_i, T) = \frac{\delta F(D_i, T)}{\delta D_i} \end{cases} \quad (6)$$

Repeating this process, a depth can be computed for each diameter and age. The rate of depth decrease, which we would refer to as obliteration rate (*r* in m/Ga), is then computed. In this analysis, we do not assume an initial morphology (depth/Diameter ratio) of the craters, which is poorly constrained, while we estimate the obliteration rate (rate of depth decrease) directly from the dataset.

In order to remove artifacts induced by scarce data and by our workflow, we applied two filters. First, due to the use of a kernel estimator, densities are computed beyond the range of observed values. In order to exclude obliteration rates computed with those densities, we computed an alpha-shape curve from our data set $\mathbb{C}$. Alpha-shape curve delineates the limit of the cloud of points in diameter-depth space. It is computed using a Delaunay triangulation, where every triangle with an edge longer than a given threshold (0.001 in our case) is then deleted.

The second filter removes obliteration rates computed in part of the CSDFD where the number of craters is too small. We computed the square root of the inverse depth cumulative density distribution in order to mimic a Poisson error (Arvidson et al., 1979). We set the error threshold to *I=0.2*, below which the obliteration rate is excluded.

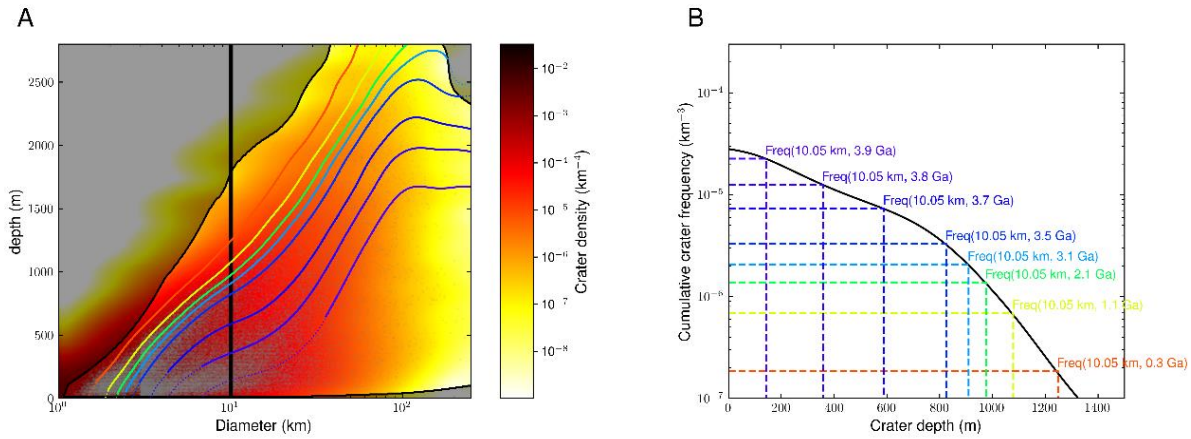

Figure 2: Explanation of the computation of crater obliteration rate. A: the crater density is plotted as the colormap. Data range not used in the computation is greyed. Colored lines represent isochrons, i.e. the depth to diameter relation of crater of a given age. B: For each diameter bin, an inverse cumulative crater frequency is computed (black line). Using cratering model, expected frequencies are computed for each time step (colored dashed lines). The result is a depth diameter relation for each time step (colored lines, also shown in A as previously mentioned). The obliteration rate is finally computed as the derivative of the depth relative to the age. Crater dataset used here comes from (Robbins and Hynek, 2012b).

2.3 Data

Many morphometric parameters can describe the shape of a crater, providing clues on processes undergone by the crater since its formation. A commonly used parameter is the depth of craters, often found as the depth to diameter ratio (d/D) (Garvin and Frawley, 1998; Golombek et al., 2006; Martellato et al., 2017; McEwen et al., 2005; Robbins and Hynek, 2012a; Stepinski et al., 2009; Warner et al., 2010; Watters et al., 2015; Wood and Andersson, 1978). This parameter is quite simple to interpret, as surface processes tend to erode the rim and fill the depression. There is no established definition for crater depth (Robbins et al., 2018b). In this study, we used the difference between the median rim elevation and the average floor elevation. This definition allows to register both erosion of the rim and infilling of the cavity.

Several Martian crater databases exist in the literature (Barlow et al., 2006; Robbins and Hynek 2012ab). To this date, Robbins and Hynek (2012b, 2012a) provides the more complete database down to 2 km in diameter with morphometry measurements on craters down to 3 km. We used the floor elevation and the median rim elevation parameters from the global crater data base to compute the depth of the craters.

197 However, many craters of less than 10 km of diameter do not have such morphometric
198 information. Table 1 summarizes the percentage of craters with morphometric information
199 available in the database, according to their diameter.
200

Diameter (km)	3 < D < 4	4 < D < 5	5 < D < 6	6 < D < 10	10 < D
Percentage of craters with morphometric information	68	77	85	90	96

201 *Table 1: the percentage of craters with morphometric information available in the Martian crater database* (Robbins and
202 Hynek, 2012b).

203 In order to study spatial variations of the CSDFD of Martian terrains, we divided the
204 surface of Mars into several areas. We used a modified version of the geologic map from
205 Tanaka et al. (2014) to delineate surfaces with different age and geologic background.
206 In the map of Tanaka et al. (2014), large Amazonian craters are mapped separately as
207 "Impact Units". These units were merged to their underlying units, when it was possible to
208 identify it, so that the CSDFDs of the surfaces include these Amazonian craters. To increase
209 the number of craters used in our analysis we merged several units. Noachian terrains are
210 merged in a single unit, we regrouped the volcanic units according to their volcanic provinces.
211 Geologic surfaces with a resurfacing history such as channel outflows or transition units are
212 kept as separate units. The final map is displayed on figure 3.
213

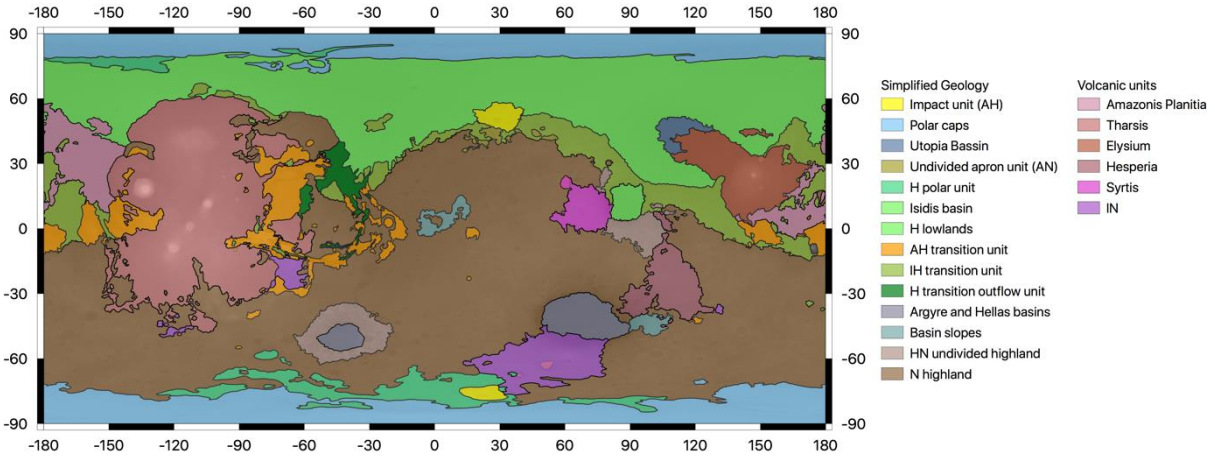

214
215 *Figure 3: Map of the studied areas. Tanaka (2014) geologic map has been used as a base. We included the impact units in the*
216 *underlaying units and regrouped some geologic units to work on larger area with better crater statistics (AH: Amazonian and*
217 *Hesperian, AN: Amazonian and Noachian, H: Hesperian, lH: late Hesperian, HN: Hesperian and Noachian, N: Noachian, lN:*
218 *late Noachian).*

Specifically, we investigated the crater size-depth frequency in the following units:

1. The Noachian highland unit. The Noachian highlands consist of almost half of the planet's surface. This unit groups the early, middle and late Noachian units from initial map in a single unit as the initial ones were spatially scattered. its ages range from 4.2 to 3.8 Ga (Carr and Head, 2010). This unit is heavily cratered, with abundant evidence for liquid water on the surface, as evidenced by fluvial networks (Carr and Clow, 1981; Craddock and Howard, 2002; Fassett and Head, 2008a; Howard et al., 2005; Pieri, 1980; Stepinski and Collier, 2003), alluvial fans (Fassett and Head, 2008b; Palucis et al., 2014), paleolakes (Fassett and Head, 2008b; Goudge et al., 2016, 2012) and hydrated minerals (Bibring et al., 2006; Murchie et al., 2009). This fluvial activity is mainly dated from the Noachian and the early Hesperian, though some younger evidences can be found (Fassett and Head, 2008a; Gulick, 1998). Thus, the obliteration rate on this unit could shed light on the variation of fluvial processes through time.
2. Volcanic units. Volcanism is widespread on Mars and active throughout Martian history (Werner, 2009). In this work, we identify five main volcanic units, including Tharsis, Elysium, Hesperia, Syrtis, and a late Noachian volcanic unit (Malea Planum). We also highlight the Amazonis Planitia unit as a volcanic unit since it is located between Elysium and Tharsis, and thus recorded mostly the volcanic resurfacing from the surroundings. Apparently, volcanism and infill of lava flows would be the most important geologic processes in these units that affect crater obliteration.
3. The northern plains: The northern lowlands of Mars are underlain by an ancient Noachian or pre-Noachian basement (Frey et al., 2002), and experienced multiple episodes of volcanism and sedimentation, throughout Martian history (Carr and Head, 2003; Pan et al., 2017). For this analysis we included most of the lowlands as the Hesperian lowlands unit, but delineated the Amazonis unit due to its close proximity to Elysium and Tharsis volcanoes.

3. Synthetic tests

To assess our method's accuracy and sensitivity to the different hypotheses made, we performed synthetic tests. We modeled crater populations with known obliteration rates, built CSDFD and measured obliteration rates using the method above described (details on modeled population generation is given in the supplementary material).

Figure 4 presents the result for a model population with a fixed initial depth and where craters are degraded according to equation 5. The erosion model is the same as what we assume in our interpretation. The computed obliteration rates accurately retrieve the intensity and timing of the input obliteration rates (Figure 4). High obliteration rates are generally more precise than low obliteration rates. However, the highest obliteration rates at older ages (e.g., >2 Ga) cannot be computed. This is explained because most craters older than the threshold ages have been totally erased. The method detects the timing of brutal changes in obliteration; however, the intensity of single resurfacing event is spread over a longer period.

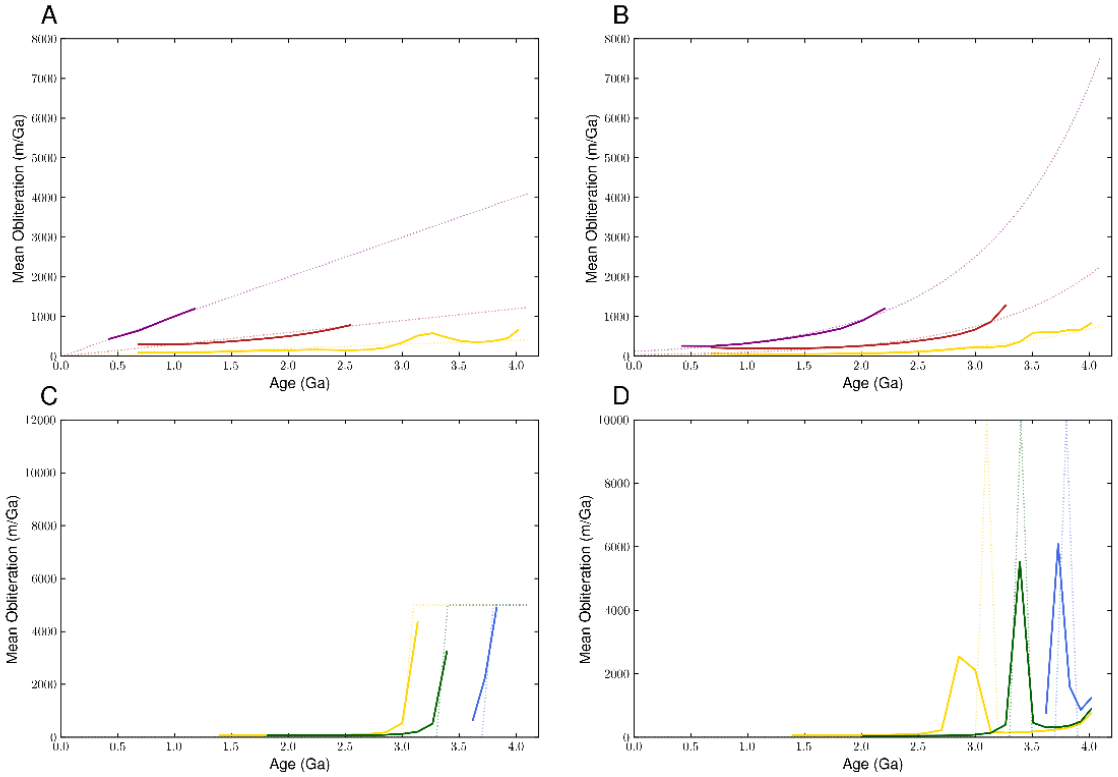

Figure 4: Synthetic tests comparing computed obliteration rates to known input rates. Input obliteration rates are represented as dotted lines. Plain lines represent the mean obliteration rates of craters between 9 and 11 km in diameter computed using our method. A. Obliteration rate is proportional to age, each color represents a different obliteration intensity. B. Obliteration rate is proportional to the exponential of the age, each color represents a different obliteration intensity. C. Obliteration rates dramatically decrease during Hesperian, each color represent a different timing for the stop of obliteration. D. One-time resurfacing event with a pic of obliteration during Hesperian, each color represents a different timing for the pic.

Figure 5 presents the result for a model including backwasting, with an increase in diameter proportional to the decrease in depth according to equation 7 (Ivanov, 2018).

$$\frac{D_t}{D_0} = \left(\frac{\frac{d_0}{D_0} - 4/3 \left(\frac{d_0}{D_0}\right)^3}{\frac{d_t}{D_t} - 4/3 \left(\frac{d_t}{D_t}\right)^3} \right)^{1/3} \quad (7)$$

Backwasting introduces an underestimation of the obliteration rates. For older ages, obliteration is computed from shallow craters that have an initial diameter smaller than the one used to compute the theoretical distribution of craters. Hence, the cratering rate is overestimated, leading to an underestimation of the obliteration rates. This underestimation increases with total obliteration, as the proportion of craters with smaller initial diameter increase in the diameter bin used to compute obliteration rate. Hence, measured obliteration rates in the first Ga are within 20% of the input rates.

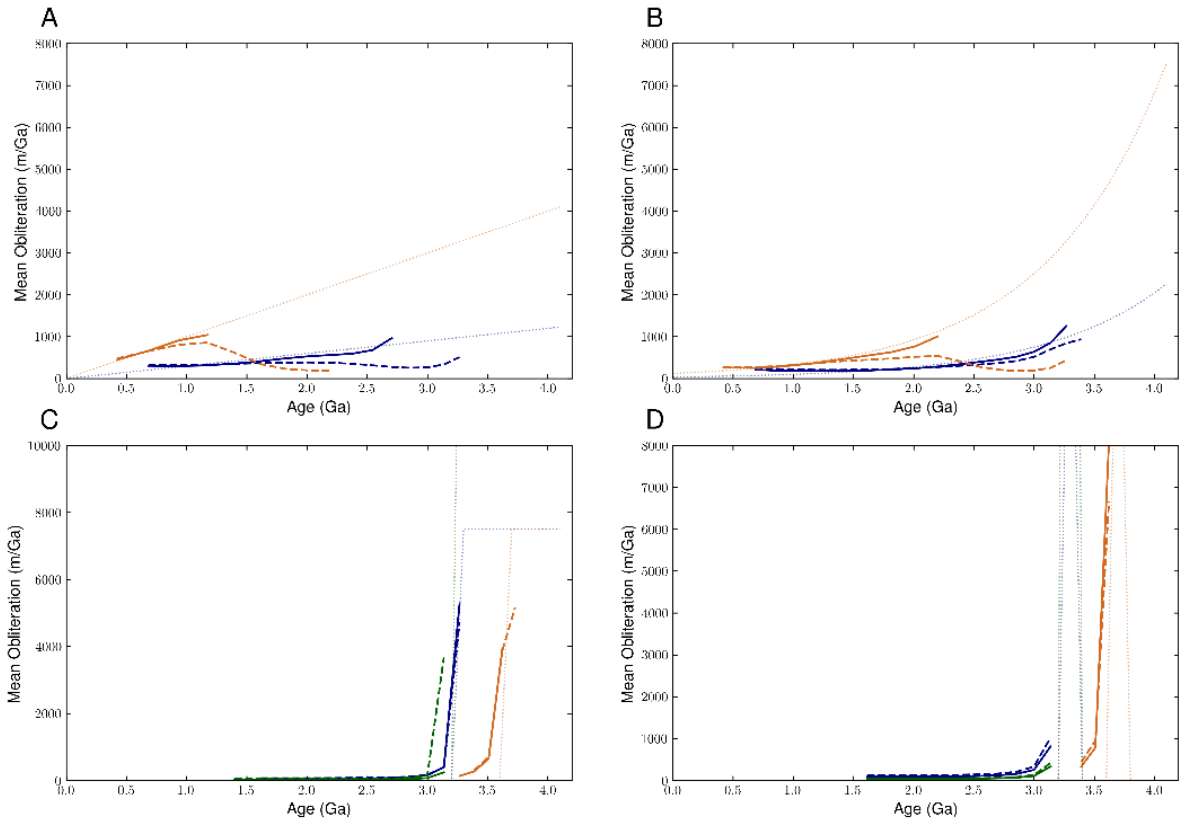

Figure 5: Synthetic tests comparing computed obliteration rates to known input rates. Input obliteration rates are represented as dotted lines. Plain and dashed lines represent the mean obliteration rates of craters between 9 and 11 km in diameter computed using our method. For plain lines, diameter of modeled craters remains constant. For dashed lines, a model of the increase of diameter with the degradation of crater is used to build the synthetic populations. A. Obliteration rate is proportional to age, each color represents a different obliteration intensity. B. Obliteration rate is proportional to the exponential of the age, each color represents a different obliteration intensity. C. Obliteration rates dramatically decrease during Hesperian, each color represent a different timing for the stop of obliteration. D. One-time resurfacing event with a pic of obliteration during Hesperian, each color represents a different timing for the pic.

Figure 6 presents the result for a model population where depth of fresh crater presents an increasing variability. The chosen erosion model is again the simplest one with a decrease of depth with time (equation 5). Fresh depth variability is expected to have an influence on measured obliteration rates as they are computed from depth distribution of craters.

Introducing an initial depth variability of 20% does not change much the computed obliteration rates. However, with a variability of 50%, several artifacts can be identified. First the apparition of a base level obliteration rate, even with an input obliteration set to 0 m/Ga, an obliteration of several hundred of m/Ga is measured. The second effect is an increase of recent obliteration rates younger than 1 Ga. This second effect is still observed for lower initial depth variability.

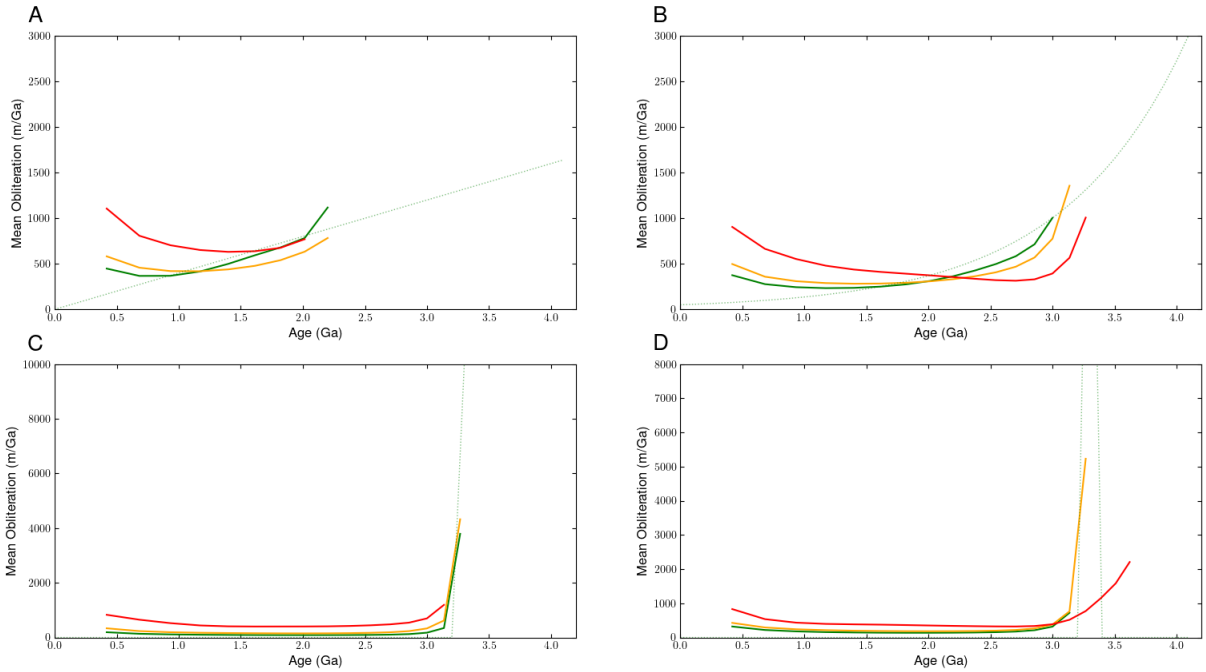

Figure 6: Synthetic tests comparing computed obliteration rates to known input rates. Input obliteration rate is the dotted line. Populations are built with different initial depth variabilities, increasing from green to red (green 10% variability, orange 20% and red 50 %). A. Obliteration rate is proportional to age. B. Obliteration rate is proportional to the exponential of the age. C. Obliteration rates dramatically decrease during Hesperian. D. One-time resurfacing event with a pic of obliteration during Hesperian.

Synthetic tests were used both to assess the precision of our method and to calibrate filters such as *l* parameter. We then computed the obliteration rates to study Martian obliteration rates.

4. Applications to Martian datasets

4.1. Highlands

Figure 7 presents the obliteration rates computed for the Noachian highland. We were able to compute obliteration rates up to 4 Ga, beyond which there is not enough craters. Above 3.7 Ga, obliteration rates are only computed for the larger diameters, because most of the craters of less than 20 km of diameter have been totally erased by resurfacing processes.

On the other hand, recent obliteration rates cannot be computed on the largest craters as the number of large young craters is insufficient to perform our computations.

The highest obliteration rates on the Highlands, around 10,000 m/Ga, are observed before 3.8 Ga, only for large craters (Figure 7A). From 3.8 Ga to 3.2 Ga, obliteration rates decrease down to 1000 m/Ga. After 3 Ga, obliteration rates remain constant below 100 m/Ga. For very recent ages, i.e., less than 1 Ga, the apparent increase in obliteration rate is explained as a methodological bias which will be discussed in section 5.1.

To better visualize the temporal variations of obliteration rates, we also represented the evolution of the obliteration rates for craters between 9 and 11 km of diameter (Figure 7B). This range has been chosen as it provides the most complete record of obliteration in time. This curve shows a dramatic decrease of obliteration rates during the Hesperian, from 2500 m/Ga at 3.8 Ga to less than 100 m/Ga at 3.2 Ga.

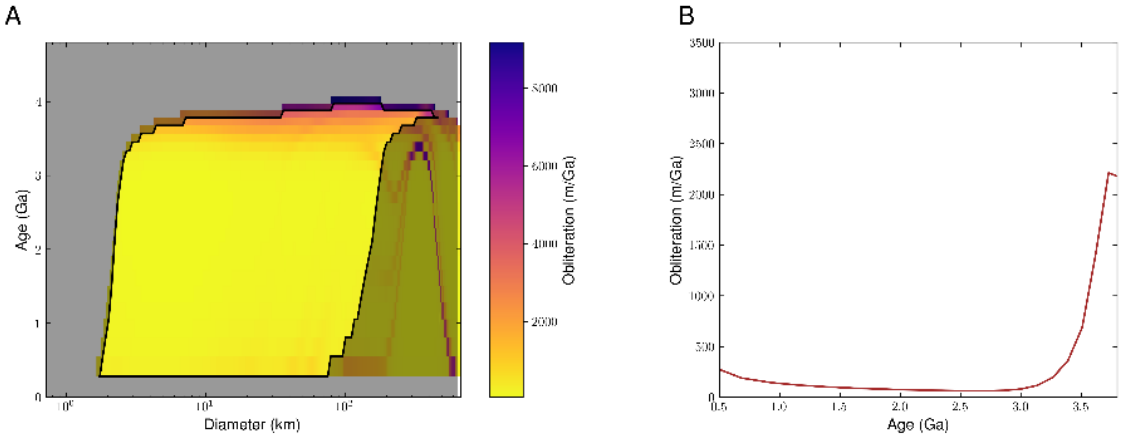

Figure 7: Obliteration rates of craters computed on the Noachian Highlands unit. 57,333 craters were used on a surface of 63 x 10^6 km^2. A: The obliteration rates are shown relative to the age and the diameter using the color scale. Darkened area represents the results excluded by our filters. B: The mean obliteration rates of craters between 9 and 11 km in diameter is represented relative to time.

4.2. Volcanic provinces

Tharsis is the biggest Martian Volcanic province. Its surface is dated from late Noachian to Amazonian (Werner, 2009). Figure 8 presents the obliteration rates computed for the Tharsis province. We only retrieve obliteration rates younger than 3.5 Ga, due to limit in crater densities. The obliteration rate quickly decreases from 3000 m/Ga to about 100 m/Ga. However, the end of the decline occurs later, reaching less than 100 m/Ga around 2.7 Ga instead of 3.2 Ga for the Noachian Highlands unit.

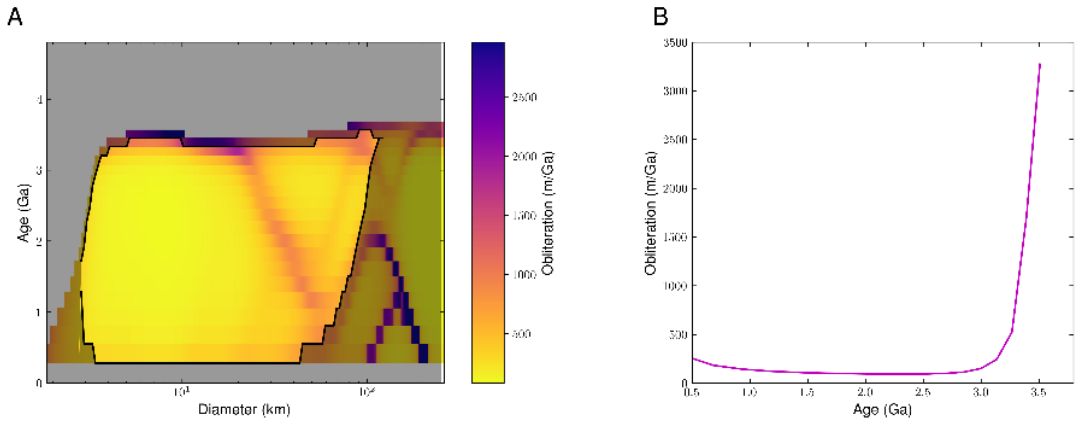

Figure 8: Obliteration rates computed on the Tharsis province unit. 2970 craters were used on a surface of 18 x 10^6 km^2. A: The obliteration rates are shown relative to the age and the diameter using the color scale. Darkened area represents the results excluded by our filters. B: The mean obliteration rates of craters between 9 and 11 km in diameter is represented relative to time.

Figure 9 presents the obliteration computed for Amazonis Planitia which is one of the youngest Amazonian volcanic units (Carr and Head, 2010). The maximum obliteration rates are much smaller than the Noachian highlands unit and Tharsis, with a maximum of 700 m/Ga. It is interesting to note that the oldest computed obliteration rates are older than the unit itself, as craters buried under the unit are included in the database. During the Amazonian however, obliteration rates are around 300 m/Ga, which is higher than on most of Mars surface at the same time (figure 11).

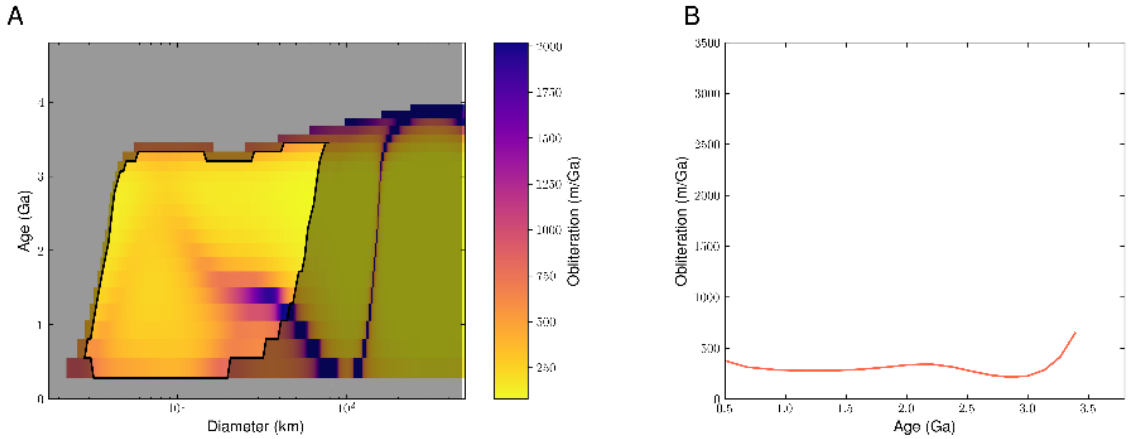

Figure 9: Obliteration rates computed on the Amazonis Planitia unit. 514 craters were used on a surface of 4 x 10^6 km^2. A: The obliteration rates are shown relative to the age and the diameter using the color scale. Darkened area represents the results excluded by our filters. B: The mean obliteration rates of craters between 9 and 11 km in diameter is represented relative to time.

Obliteration rates measured on Tharsis and Amazonis present changes with the diameter. On Tharsis, obliteration rates peak at crater diameter between 20 and 30 km and the peak shifts toward bigger craters from 3 to 1.5 Ga. A similar observation can be made on Amazonis Planitia for craters between 8 and 20 km. This observation is not yet well understood. Further work will help determinate if this results from an artifact or if this is specific to volcanic areas.

4.3. Northern Lowlands

Figure 10 presents the obliteration computed for the Hesperian lowlands unit. Obliteration rates are computed up to 3.5 Ga and decrease exponentially with time like what is observed on the units previously described. However, after displaying low obliteration rates from 3 to 1.8 Ga, obliteration increases again reaching a rate of about 500 m/Ga. This value is the highest obliteration rate observed on Mars during the Amazonian and corresponds well to the timing and depth of VBF deposit previously inferred from the crater density of buried impact craters (Head et al., 2002).

Once again, our method not only computes obliteration rates for the most surficial geologic units, since 1.5 Ga, but also retrieves information from the underlying buried craters, as seen here with obliteration rates before 3 Ga.

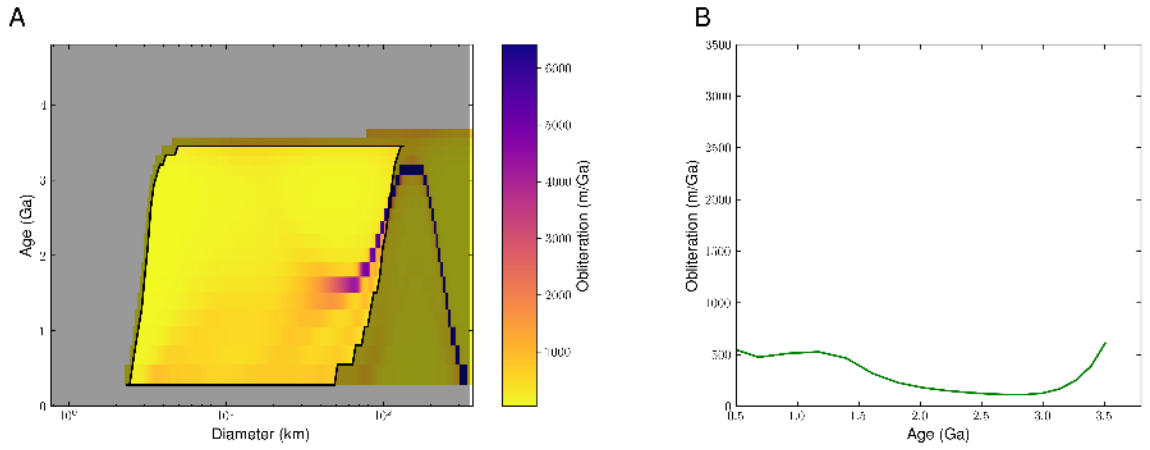

Figure 10: Obliteration rates computed on the Hesperian lowlands unit. 4082 craters were used on a surface of 19 x 10^6 km^2. A: The obliteration rates are shown relative to the age and the diameter using the color scale. Darkened area represents the results excluded by our filters. B: The mean obliteration rates of craters between 9 and 11 km in diameter is represented relative to time.

380 *4.4. Global scale*

381 Figure 11 presents the evolution of obliteration on Mars at a global scale from the late
382 Noachian to the Amazonian. The displayed obliteration is computed as the mean value
383 observed between 9 to 11 km of diameter. The map offers a better view of spatial variations
384 of obliteration rates on Mars, while plotting the obliteration relative to the age offers insight
385 in long term variation of Mars obliteration rates.

386 Above 3.7 Ga, only few geologic surfaces are old and big enough to estimate
387 obliteration rates, namely Noachian Highlands, Amazonian and Hesperian Transition unit and
388 late Hesperian transition unit. In this timespan obliteration rates are steady around 3000
389 m/Ga. From 3.7 Ga to 3.2 Ga obliteration rates decrease down to few hundreds of m/Ga.
390 During this period, obliteration rates present high spatial variations with Argyre slope unit and
391 Hellas slope unit having still obliteration rate up to 3000 m/Ga at 3.6 Ga. After 3.2 Ga,
392 obliteration rates reach values close to 0 m/Ga except in the case of Amazonian Lowlands.

393 Geologic units related to volcanic processes present a slightly different variation of
394 obliteration rates. The oldest retrieved obliteration rates are the most important for each unit.
395 Then, in a few hundreds of Ma, obliteration rates decrease down to a few hundreds of m/Ga.
396 Each unit presents a different timing: Syrtis, Hesperia, Isidis and Tharsis, from the oldest to
397 the youngest.

398 We show that the obliteration rates in general decrease with time on Mars with the
399 exception of Hesperian lowlands unit during Amazonian. During the Hesperian, volcanic
400 provinces like Tharsis, Syrtis and Hesperia present high obliteration rates ranging from 1000
401 to 3000 m/Ga. Amazonis Planitia, located between two largest volcanic provinces (Elysium
402 and Tharsis) also shows an increase in obliteration rates around 2.0 Ga, likely due to
403 Amazonian volcanism which filled this plains unit.

404 Our results show that on Mars the processes that obliterate craters occur at different
405 epochs in spatially distinct units. Our findings are consistent with previous estimates on crater
406 obliteration rates in the Noachian highlands (Carr, 1992; Grant et al., 2006; Quantin-Nataf et
407 al., 2019), the timing of the activity of large volcanic provinces (Werner, 2009), as well as the
408 geologic history of the northern lowlands (Carr and Head, 2003). In addition, our work
409 presents a continuous function of the obliteration rate through time based on crater size and
410 depth statistics, providing new information on the geologic processes in smaller provinces
411 (e.g. Amazonis) that may not be obvious in previous studies. This analysis also presents the

absolute values of obliteration rates so the amplitude of geological processes could be compared. For example, we showed that the obliteration rates in the Hesperian age volcanic provinces, likely due to volcanic infilling, is more significant compared to those obliteration rate in Noachian terrains, possibly due to fluvial activity.

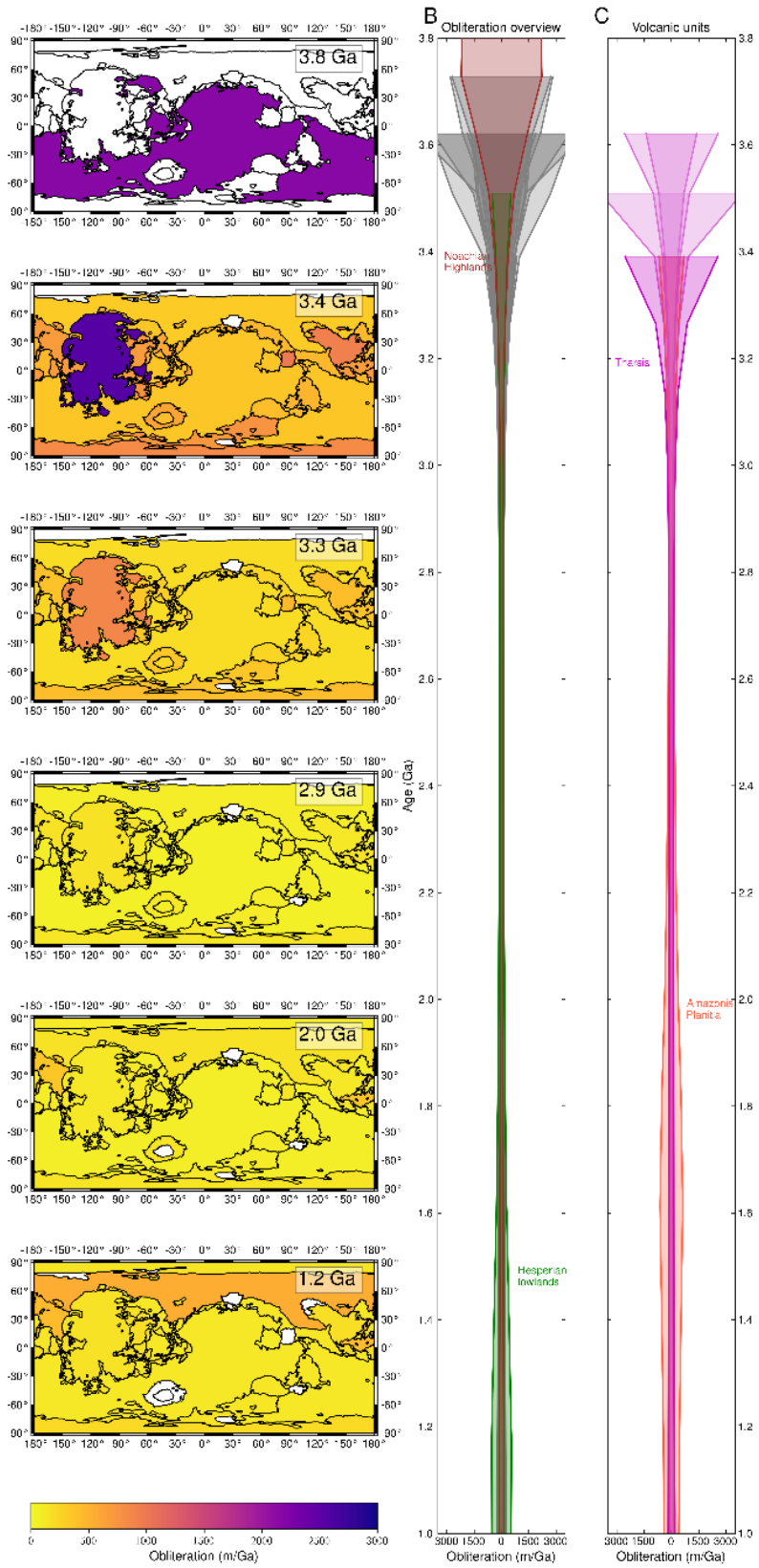

Figure 11: Evolution of the obliteration rates during Mars history at a global scale. Displayed obliteration rate is the mean value of crater obliteration rates between 9 to 11 km in diameter. A. Global map showing the evolution of obliteration rates with time. White is displayed where obliteration rates cannot be computed. B. and C. obliteration rates comparison between different areas. B. For geologic unit except volcanic units which are represented on C.

5. Discussion

5.1 Validation and limit of the method

Our starting hypothesis was that crater population would be better represented using a 3D CSDFD in diameter, depth and frequency rather than the usual 2D CSFD. The method developed in this study aims to build and interpret those CSDFDs. We show here that, from a crater map associated with morphometry information, we were able to trace the obliteration history of the mapped surface using the CSDFD representation and cratering models.

5.1.1 Limitation due to Kernel estimator

Computing crater frequency in 3D is more difficult than classic CSFD. It requires a greater number of craters, as we need good statistics in both diameter and depth dimension. Using kernel estimators has proven useful to produce a continuous representation of crater frequency in diameter-depth space.

The method proposed by (Robbins et al., 2018a) opens a new field for crater representation. However, many improvements are still possible. To better represent the crater density, it may be possible to improve the current CSDFD, using adaptative kernel estimator and mirroring methods. Those two approaches could help reduce the rollover observed at the border of the distribution when the actual decrease in number density is more important than the kernel shape (as shown in Robbins et al. (2018a)). A better understanding of processes that shape CSDFD along with a better estimation of analytical errors will help build better representations.

Increasing the number of craters used to build the CSDFD improve the quality of the computed kernel. Hence, increasing the size of the data set, by including smaller diameter craters could provide a better time resolution, especially during Amazonian when the impact flux was lower.

Construction of CSDFDs from a population of craters remains difficult, as diameter, depth and frequency have ranges crossing several orders of magnitude. The steep decrease in frequency when reaching shallow depths is poorly passed to CSDFDs, which results in the lost of information on the oldest craters. Therefore, the obliteration rates are less likely to be retrieved. To circumvent this issue, further work should focus on building models of CSDFDs that can predict the frequency of crater for a given diameter, depth, age and obliteration

455 history. Those models could later be compared with observed population with a probabilistic
456 approach similar to the one proposed by Michael et al., 2016.
457
458 *5.1.2 Validation and limits of the method: synthetic tests*
459 Synthetic tests presented in section 3 and in the supplementary material show that,
460 given known impact flux and obliteration model, our method is efficient to retrieve absolute
461 values of obliteration rates along with its change in time with good accuracy.
462 It is difficult to provide an error for the measured obliteration rates as we cannot
463 predict the exact geologic processes that result in crater degradation. Synthetic tests show
464 that backwasting leads to an underestimation of the measured obliteration rates. This error
465 can reach a factor of two when the obliteration rates remain high during several billions of
466 years. Variability of the depth of fresh craters can also have an influence, increasing
467 obliteration rates for ages lower than 2 Ga.
468 Although those effects can be significant, we expect obliteration rates we measured
469 on Mars to be accurate enough to be interpreted. Backwasting artifacts are unlikely as
470 synthetic tests similar to Mars results (e.g. with a steep decrease of obliteration rates few
471 billion years ago) are not strongly modified compared to input obliteration rates. Variability
472 of the depth of fresh craters has, probably, a stronger effect. Similar to synthetic tests, we
473 observe an increase of obliteration for recent ages (<1-1.5 Ga) and base level obliteration
474 rates. The recent increase in obliteration rates remains small enough, and we considered
475 other sides effects of fresh depth variability to be negligible.
476 Our method could be improved by considering more complicated processes. As shown
477 in the synthetic tests (figure 5), considering backwasting will be critical to better constrain long
478 lasting obliteration rates. A better understanding of crater populations and initial shape of
479 crater could also enhance computed obliteration rates.
480 Additionally, the model presented here used the simplistic model of crater
481 degradation, as an illustration of the CSDFD methodology. Different degradation processes
482 (e.g., eolian or fluvial deposition or erosion) imply different equations for modeling the crater
483 morphometry evolution. Therefore, using forward modeling of crater size and depth
484 frequency distribution, one can eventually try to retrieve the processes that created a given
485 state of degradation. The potential application would be explored in future studies.
486

5.1.3 Validation and limits of the method: actual data application

Obliteration rates computed from CSDFD compare very well with values found from other approaches. On Mars, Noachian obliteration rates are estimated around several thousands of m/Ga, similar to our results (Carr, 1992; Craddock et al., 1997; Golombek and Bridges, 2000; Quantin-Nataf et al., 2019). Our measured Amazonian obliteration rates, around 100 m/Ga, are larger than literature values, that range from tens of meters/Ga (Carr, 1992; Farley et al., 2013; Palucis et al., 2014) to less than 1 m/Ga (Golombek et al., 2014; Grant et al., 2006). This discrepancy can be explained two factors. First, we reach the resolution limit of our method: the precision of depth measurements is less than the expected variation for very low obliteration rates. Second, since our method monitors obliteration rates at different time scales, the unsteadiness of obliteration processes can thus explain this variation. Higher resolution dataset will be more appropriate to study obliteration variation during the Amazonian.

As seen in figures 7 and 8, very recent obliteration rates, i.e., less than 1 Ga old, increase up to several hundreds of kilometers/Ga. Increasing the error threshold *l* to higher values than 0.2 reduces this effect. However, increasing *l* will also remove too much information on some surfaces as this effect seems to increase for larger area. From data and synthetic tests, we set *l=0.2* as it provided a good compromise between the artifact intensity and the loss of information on smaller surfaces.

Oldest obliteration rates are often computed with few craters, as the oldest craters are erased from the surface, and it is thus difficult to retrieve Noachian obliteration rates, especially for craters less than 20 km in diameter.

Classic crater dating is using all craters observed on a surface as related to its subsequent exposition to the bombardment. But in some case, older craters emplaced on buried layers are still visible, like the quasi-circular depressions in the northern lowlands. Here, our method is free from this limitation. As illustrated by the cases of the Northern lowlands and Amazonis Planitia, we were able to retrieve not only obliteration of the surficial unit but also of the buried unit. This could also prove useful in the case of a unit with a continuous emplacement, e.g., a lava flow unit, as we trace the activity of the surface from start to the end of the emplacement rather to give a single age.

It is hard to assess the resolution of our method in time and intensity of obliteration. First source of error is the cratering model that lacks anchor points on Mars, resulting in very

large uncertainties on absolute ages provided by crater dating and thus on the intensity and timing of our estimated obliteration rates. Unless future sample returns provide absolute ages of the surface rocks, the computed obliteration rates estimated using the CSDFD presentation above provide the best possible analysis given present knowledge of Martian chronology.

5.2 Interpretation of the CSDFD of Mars database

5.2.1 Noachian obliteration rates

Noachian obliteration can only be computed on the oldest and largest units. However, the computed values are in compliance with previous studies. Our method offers a quantitative measurement of crater obliteration without specifying the geologic process. It would require more detailed morphometry measurements and models to estimate the nature of the processes that obliterated the craters.

Such high obliteration rates in the Noachian (several thousands of m/Ga) can be produced either by cratering, erosion and sedimentation or volcanism. In order to discriminate those processes, further work is needed to investigate the different crater morphometry, e.g., the increase in diameter and reduction in rim height during erosional processes. Investigating the area with supplementary geomorphologic tools will clarify the processes at work. Including more complex models for the different processes may also result in better interpretation of the CSDFD.

Increasing the number of used craters, mapping down to 1 km of diameter, using the High-Resolution Stereo Imager (HRSC), could help having a better view on the Hesperian and Amazonian obliteration rates. However, a complete mapping including smaller craters would involve a very high number of craters. Automated crater mapping methods would be desirable for such types of studies.

5.2.2 Volcanism

Obliteration rates on volcanic province units stand apart with obliteration rates one order of magnitude higher than on the rest of Mars (Figure 11). The highest obliterations rates associated to these volcanic provinces coincide with their known activity (Carr and Head, 2010; Werner, 2009). However, as previously mentioned in the method section (Section 2.1), rather than providing a single age for a surface, our method gives a continuous information in time about the activity of the surface.

Transforming crater obliteration in term of volume of lava emitted, our method could be used to better track the volcanic activity of Mars, which could provide precious insight on the thermal evolution of Mars. For these analyses, higher resolution maps could also provide better obliteration rates, especially for recent activity such as on Olympus Mons or Amazonis Planitia.

5.2.3 Northern Lowlands

Northern lowland presents an abnormally high obliteration rate from 1.5 Ga to present. This result is very interesting in many regards. This high rate is unexpected as Amazonian surface activity is quite low. Several hypotheses can be proposed to account for those obliteration rates. The first is infilling with lava flow. However, the timing and intensity of the obliteration are different from Amazonis Planitia, and there is no known large-scale volcanic activity operating during this time period. The second explanation can be infilling with aeolian processes. Indeed, large dune fields (Olympus Undae) are observed around the north polar cap (Tanaka et al., 2005). But it is unlikely that only aeolian processes account for this amount of obliteration (Grant et al., 2006). Aqueous sedimentation would be able to produce the observed obliteration intensities, but we do not expect large scale aqueous activities on Mars based on the observations of fluvial morphology globally (Carr and Head, 2010).

Another explanation can be linked with the presence of ice on the surface. High latitudes of Mars are known to contain ice (Boynton et al., 2002; Feldman, 2002; Mellon et al., 2009; Smith et al., 2009). This increase could be linked to the accumulation of ice in the craters. Our method could then give precious insight on the activity of Martian cryosphere during Amazonian.

Finally, we note that our identification of the elevated obliteration rate is likely consistent with the prior geologic interpretation of the emplacement of the Vastitas Borealis Formation (VBF) that covers most of the Northern lowlands (Tanaka et al., 2005). This origin of the VBF formation is still not well understood. The age dating of the Vastitas Borealis Formation ranges from the Hesperian (Kreslavsky and Head, 2002) to the Amazonian (Tanaka et al., 2005). This discrepancy in proposed ages is linked with the high degradation state of craters. Our results seem to favor an Amazonian age with a continuous formation starting 1.5 Ga ago. The obliteration rates of the impact craters in the northern lowlands may be used to provide further insights into the origin of this recent geologic unit.

Conclusion

We propose here a brand-new method that can retrace the obliteration history of a crater population of known depth. Using the crater size-depth-frequency (CSDFD) representation, we can now provide constraints of continuous obliteration of craters on any surface with topographic information and a known impactor flux without additional assumption on the initial crater shape. This method is based on a new representation of scattered crater size-depth dataset, providing continuous crater frequency according to depth and diameter. Obliteration rate can be computed as a function of time given different size populations.

As we implemented this methodology to a global Martian dataset, our method provided important new observations on Martian obliteration rates: quantifying Noachian obliteration rates, tracing volcanic activity, and revealing high rate of Amazonian surface activity on the Northern Lowlands. We also identified the volcanic activity in the Hesperian age presents a much higher obliteration rate than any other units during other epochs.

Further development will include better obliteration models along with proper inversion between data (CSDFD) and models. Increasing the resolution of the crater map will also provide better quantification and time resolution along with a constrain on the processes at stake.

Obliteration rate analysis as we presented using CSDFD is useful to evaluate erosion rate, as well as how long a surface was exposed to UV radiation, with astrobiology implications. Extending our field of study to other planetary bodies such as the Moon or icy satellites could provide exciting new results on their geologic and surface evolution.

Bibliography

Arvidson, R.E., Boyce, J.M., Chapman, C.R., Cintala, M., Fulchignoni, M., Moore, H., Neukum, G., Schultz, P., Soderblom, L.A., Strom, R.G., Woronow, A., Young, R., 1979. Standard techniques for presentation and analysis of crater size-frequency data. Icarus 37, 467–474. https://doi.org/10.1016/0019-1035(79)90009-5

Baldwin, R.B., 1949. The face of the moon. [Chicago] Univ. Chicago Press [1949].

Barlow, N.G., 2005. A review of Martian impact crater ejecta structures and their

613 implications for target properties, in: Large Meteorite Impacts III. Geological Society of
614 America, pp. 433–442. https://doi.org/10.1130/0-8137-2384-1.433
615 Bibring, J.P., Langevin, Y., Mustard, J.F., Poulet, F., Arvidson, Raymond, Gendrin, A., Gondet,
616 B., Mangold, N., Pinet, P., Forget, F., Berthe, M., Gomez, C., Jouglet, D., Soufflot, A.,
617 Vincendon, M., Combes, M., Drossart, P., Encrenaz, T., Fouchet, T., Merchiorri, R.,
618 Belluci, G.C., Altieri, F., Formisano, V., Capaccioni, F., Cerroni, P., Coradini, A., Fonti, S.,
619 Korablev, O., Kottsov, V., Ignatiev, N., Moroz, V., Titov, D., Zasova, L., Loiseau, D., Pinet,
620 Patrick, Douté, S., Schmitt, B., Sotin, C., Hauber, E., Hoffmann, H., Jaumann, R., Keller,
621 U., Arvidson, Ray, Duxbury, T., Forget, François, Neukum, G., 2006. Global mineralogical
622 and aqueous Mars history derived from OMEGA/Mars express data. Science (80-.). 312,
623 400–404. https://doi.org/10.1126/science.1122659
624 Boynton, W. V., Feldman, W.C., Squyres, S.W., Prettyman, T.H., Brückner, J., Evans, L.G.,
625 Reedy, R.C., Starr, R., Arnold, J.R., Drake, D.M., Englert, P.A.J., Metzger, A.E.,
626 Mitrofanov, I., Trombka, J.I., D'Uston, C., Wänke, H., Gasnault, O., Hamara, D.K., Janes,
627 D.M., Marcialis, R.L., Maurice, S., Mikheeva, I., Taylor, G.J., Tokar, R., Shinohara, C.,
628 2002. Distribution of hydrogen in the near surface of Mars: Evidence for subsurface ice
629 deposits. Science (80-.). 297, 81–85. https://doi.org/10.1126/science.1073722
630 Carr, M.H., 1992. Post-Noachian Erosion Rates: Implications for Mars Climate Change, in:
631 Lunar and Planetary Science Conference. pp. 205–206.
632 Carr, M.H., Clow, G.D., 1981. Martian channels and valleys: Their characteristics, distribution,
633 and age. Icarus 48, 91–117. https://doi.org/10.1016/0019-1035(81)90156-1
634 Carr, M.H., Head, J.W., 2010. Geologic history of Mars. Earth Planet. Sci. Lett. 294, 185–203.
635 https://doi.org/10.1016/j.epsl.2009.06.042
636 Carr, M.H., Head, J.W., 2003. Oceans on Mars: An assessment of the observational evidence
637 and possible fate. J. Geophys. Res. E Planets 108.
638 https://doi.org/10.1029/2002je001963
639 Craddock, R.A., Howard, A.D., 2002. The case for rainfall on a warm, wet early Mars. J.
640 Geophys. Res. E Planets 107, 21-1-21–36. https://doi.org/10.1029/2001JE001505
641 Craddock, R.A., Maxwell, T. a., Howard, A.D., 1997. Crater morphometry and modification in
642 the Sinus Sabaeus and Margaritifer Sinus regions of Mars. J. Geophys. Res. 102, 13321.
643 https://doi.org/10.1029/97JE01084
644 Daubar, I.J., Atwood-Stone, C., Byrne, S., McEwen, A.S., Russell, P.S., 2014. The morphology

of small fresh craters on Mars and the Moon. J. Geophys. Res. Planets 119, 2620–2639. https://doi.org/10.1002/2014JE004671

Daubar, I.J., McEwen, A.S., Byrne, S., Kennedy, M.R., Ivanov, B.A., 2013. The current martian cratering rate. Icarus 225, 506–516. https://doi.org/10.1016/j.icarus.2013.04.009

Farley, K.A., Malespin, C., Mahaffy, P., Grotzinger, J.P., 2013. In Situ Radiometric and Exposure Age Dating of the Martian Surface — Supplementary Materials 1–9.

Fassett, C.I., Head, J.W., 2008a. The timing of martian valley network activity: Constraints from buffered crater counting. Icarus 195, 61–89. https://doi.org/10.1016/j.icarus.2007.12.009

Fassett, C.I., Head, J.W., 2008b. Valley network-fed, open-basin lakes on Mars: Distribution and implications for Noachian surface and subsurface hydrology. Icarus 198, 37–56. https://doi.org/10.1016/j.icarus.2008.06.016

Feldman, W.C., 2002. Global Distribution of Neutrons from Mars: Results from Mars Odyssey. Science (80-.). 297, 75–78. https://doi.org/10.1126/science.1073541

Frey, H. V., Roark, J.H., Shockey, K.M., Frey, E.L., Sakimoto, S.E.H., 2002. Ancient lowlands on Mars. Geophys. Res. Lett. 29, 22-1-22–4. https://doi.org/10.1029/2001gl013832

Garvin, J.B., Frawley, J.J., 1998. Geometric properties of Martian impact craters: Preliminary results from the Mars Orbiter Laser Altimeter. Geophys. Res. Lett. 25, 4405–4408. https://doi.org/10.1029/1998GL900177

Golombek, M.P., Bridges, N.T., 2000. Erosion rates on Mars and implications for climate change: Constraints from the Pathfinder landing site. J. Geophys. Res. E Planets 105, 1841–1853. https://doi.org/10.1029/1999JE001043

Golombek, M.P., Grant, J.A., Crumpler, L.S., Greeley, R., Arvidson, R.E., Bell, J.F., Weitz, C.M., Sullivan, R.J., Christensen, P.R., Soderblom, L.A., Squyres, S.W., 2006. Erosion rates at the Mars Exploration Rover landing sites and long-term climate change on Mars. J. Geophys. Res. E Planets 111, 1–14. https://doi.org/10.1029/2006JE002754

Golombek, M.P., Warner, N.H., Ganti, V., Lamb, M.P., Parker, T.J., Fergason, R.L., Sullivan, R.J., 2014. Small crater modification on Meridiani Planum and implications for erosion rates and climate change on Mars M. 2522–2547. https://doi.org/10.1002/2014JE004658.Received

Goudge, T.A., Fassett, C.I., Head, J.W., Mustard, J.F., Aureli, K.L., 2016. Insights into surface runoff on early Mars from paleolake basin morphology and stratigraphy. Geology 44,

677 419–422. https://doi.org/10.1130/G37734.1
678 Goudge, T.A., Head, J.W., Mustard, J.F., Fassett, C.I., 2012. An analysis of open-basin lake
679 deposits on Mars: Evidence for the nature of associated lacustrine deposits and post-
680 lacustrine modification processes. Icarus 219, 211–229.
681 https://doi.org/10.1016/j.icarus.2012.02.027
682 Grant, J.A., Arvidson, R.E., Crumpler, L.S., Golombek, M.P., Hahn, B., Haldemann, A.F.C., Li,
683 R., Soderblom, L.A., Squyres, S.W., Wright, S.P., Watters, W.A., 2006. Crater gradation
684 in Gusev crater and Meridiani Planum, Mars. J. Geophys. Res. E Planets 111, 1–23.
685 https://doi.org/10.1029/2005JE002465
686 Gulick, V.C., 1998. Magmatic intrusions and a hydrothermal origin for fluvial valleys on Mars.
687 J. Geophys. Res. E Planets 103, 19365–19387. https://doi.org/10.1029/98JE01321
688 Hartmann, W.K., 2005. Martian cratering 8: Isochron refinement and the chronology of
689 Mars. Icarus 174, 294–320. https://doi.org/10.1016/j.icarus.2004.11.023
690 Hartmann, W.K., 1970. Lunar cratering chronology. Icarus 13, 299–301.
691 https://doi.org/10.1016/0019-1035(70)90059-X
692 Hartmann, W.K., Neukum, G., 2001. Cratering chronology and the evolution of Mars. Space
693 Sci. Rev. 96, 165–194. https://doi.org/10.1023/A:1011945222010
694 Head, J.W., Kreslavsky, M.A., Pratt, S., 2002. Northern lowlands of Mars: Evidence for
695 widespread volcanic flooding and tectonic deformation in the Hesperian Period. J.
696 Geophys. Res. E Planets 107. https://doi.org/10.1029/2000je001445
697 Howard, A.D., Moore, J.M., Irwin, R.P., 2005. An intense terminal epoch of widespread fluvial
698 activity on early Mars: 1. Valley network incision and associated deposits. J. Geophys.
699 Res. E Planets 110, 1–20. https://doi.org/10.1029/2005JE002459
700 Ivanov, B.A., 2018. Size-Frequency Distribution of Small Lunar Craters: Widening with
701 Degradation and Crater Lifetime. Sol. Syst. Res. 52, 1–25.
702 https://doi.org/10.1134/S0038094618010021
703 Ivanov, B.A., 2001. Mars/Moon cratering rate ratio estimates. Space Sci. Rev. 96, 87–104.
704 https://doi.org/10.1023/A:1011941121102
705 Kreslavsky, M.A., Head, J.W., 2002. Fate of outflow channel effluents in the northern
706 lowlands of Mars: The Vastitas Borealis Formation as a sublimation residue from frozen
707 ponded bodies of water. J. Geophys. Res. E Planets 107, 4–1.
708 https://doi.org/10.1029/2001JE001831

709 Mangold, N., Adeli, S., Conway, S., Ansan, V., Langlais, B., 2012. A chronology of early Mars
710 climatic evolution from impact crater degradation. J. Geophys. Res. E Planets 117, 1–22.
711 https://doi.org/10.1029/2011JE004005
712 Martellato, E., Vivaldi, V., Massironi, M., Cremonese, G., Marzari, F., Ninfo, A., Haruyama, J.,
713 2017. Is the Linné impact crater morphology influenced by the rheological layering on
714 the Moon's surface? Insights from numerical modeling. Meteorit. Planet. Sci. 52, 1388–
715 1411. https://doi.org/10.1111/maps.12892
716 McEwen, A.S., Preblich, B.S., Turtle, E.P., Artemieva, N.A., Golombek, M.P., Hurst, M., Kirk,
717 R.L., Burr, D.M., Christensen, P.R., 2005. The rayed crater Zunil and interpretations of
718 small impact craters on Mars. Icarus 176, 351–381.
719 https://doi.org/10.1016/j.icarus.2005.02.009
720 Mellon, M.T., Arvidson, R.E., Marlow, J.J., Phillips, R.J., Asphaug, E., 2009. Periglacial
721 landforms at the Phoenix landing site and the northern plains of Mars. J. Geophys. Res.
722 E Planets. https://doi.org/10.1029/2007JE003039
723 Melosh, H.J., 1989. Impact cratering: A Geologic Process. https://doi.org/1989icgp.book.....M
724 Michael, G.G., 2013. Planetary surface dating from crater size–frequency distribution
725 measurements: Multiple resurfacing episodes and differential isochron fitting. Icarus
726 226, 885–890. https://doi.org/10.1016/j.icarus.2013.07.004
727 Michael, G.G., Kneissl, T., Neesemann, A., 2016. Planetary surface dating from crater size-
728 frequency distribution measurements: Poisson timing analysis. Icarus 277, 279–285.
729 https://doi.org/10.1016/j.icarus.2016.05.019
730 Murchie, S.L., Mustard, J.F., Ehlmann, B.L., Milliken, R.E., Bishop, J.L., McKeown, N.K., Noe
731 Dobrea, E.Z., Seelos, F.P., Buczkowski, D.L., Wiseman, S.M., Arvidson, R.E., Wray, J.J.,
732 Swayze, G., Clark, R.N., Des Marais, D.J., McEwen, A.S., Bibring, J.P., 2009. A synthesis of
733 Martian aqueous mineralogy after 1 Mars year of observations from the Mars
734 Reconnaissance Orbiter. J. Geophys. Res. E Planets 114.
735 https://doi.org/10.1029/2009JE003342
736 Neukum, G., Ivanov, B.A., Hartmann, W.K., 2001. Cratering records in the inner solar system
737 in relation to the lunar reference system. Space Sci. Rev. 96, 55–86.
738 https://doi.org/10.1023/A:1011989004263
739 Neukum, G., König, B., Fechtig, H., 1977. Cratering in the Earth-Moon system-Consequences
740 for age determination by crater counting. J. Geophys. Res. 82, 376–388.

741 Opik, E.J., 1966. The Martian Surface. Science (80-.). 153, 255–265.
742 https://doi.org/10.1126/science.153.3733.255
743 Palucis, M.C., Dietrich, W.E., Hayes, A.G., Williams, R.M.E., Gupta, S., Mangold, N., Newsom,
744 H.E., Hardgrove, C., Calef, F.J., Sumner, D.Y., 2014. The origin and evolution of the
745 Peace Vallis fan system that drains to the Curiosity landing area, Gale Crater, Mars 705–
746 728. https://doi.org/10.1002/2013JE004583.Received
747 Pan, L., Ehlmann, B.L., Carter, J., Ernst, C.M., 2017. The stratigraphy and history of Mars'
748 northern lowlands through mineralogy of impact craters: A comprehensive survey. J.
749 Geophys. Res. Planets 122, 1824–1854. https://doi.org/10.1002/2017JE005276
750 Pan, L., Quantin-Nataf, C., Breton, S., Michaut, C., 2019. The impact origin and evolution of
751 Chryse Planitia on Mars revealed by buried craters. Nat. Commun. 10, 4257.
752 https://doi.org/10.1038/s41467-019-12162-0
753 Pieri, D.C., 1980. Martian Valleys: Morphology, Distribution, Age, and Origin. Science (80-.).
754 210, 895–897. https://doi.org/10.1126/science.210.4472.895
755 Pike, R.J., 1980. Control of crater morphology by gravity and target type: Mars, Earth, Moon.
756 Geochim. Cosmochim. Acta, Suppl. 14, 2159–2189.
757 Pike, R.J., 1974. Depth/diameter relations of fresh lunar craters: Revision from spacecraft
758 data. Geophys. Res. Lett. 1, 291–294. https://doi.org/10.1029/GL001i007p00291
759 Plescia, J.B., Cintala, M.J., 2012. Impact melt in small lunar highland craters. J. Geophys. Res.
760 E Planets 117, 1–12. https://doi.org/10.1029/2011JE003941
761 Quantin-Nataf, C., Craddock, R.A., Dubuffet, F., Lozac'h, L., Martinot, M., 2019. Decline of
762 crater obliteration rates during early martian history. Icarus 317, 427–433.
763 https://doi.org/10.1016/j.icarus.2018.08.005
764 Robbins, S.J., Hynek, B.M., 2012a. A new global database of Mars impact craters ≥1 km: 2.
765 Global crater properties and regional variations of the simple-to-complex transition
766 diameter. J. Geophys. Res. E Planets 117, 1–21. https://doi.org/10.1029/2011JE003967
767 Robbins, S.J., Hynek, B.M., 2012b. A new global database of Mars impact craters ≥1 km: 1.
768 Database creation, properties, and parameters. J. Geophys. Res. E Planets 117, 1–18.
769 https://doi.org/10.1029/2011JE003966
770 Robbins, S.J., Riggs, J.D., Weaver, B.P., Bierhaus, E.B., Chapman, C.R., Kirchoff, M.R., Singer,
771 K.N., Gaddis, L.R., 2018a. Revised recommended methods for analyzing crater size-
772 frequency distributions. Meteorit. Planet. Sci. 53, 891–931.

https://doi.org/10.1111/maps.12990
Robbins, S.J., Watters, W.A., Chappelow, J.E., Bray, V.J., Daubar, I.J., Craddock, R.A., Beyer, R.A., Landis, M., Ostrach, L.R., Tornabene, L., Riggs, J.D., Weaver, B.P., 2018b. Measuring impact crater depth throughout the solar system. Meteorit. Planet. Sci. 53, 583–637. https://doi.org/10.1111/maps.12956
Schenk, P., Castillo-Rogez, J., Otto, K.A., Marchi, S., O'Brien, D., Bland, M., Hughson, K., Schmidt, B., Scully, J., Buczkowski, D., Krohn, K., Hoogenboom, T., Kramer, G., Bray, V., Neesemann, A., Hiesinger, H., Platz, T., De Sanctis, M.C., Schroeder, S., Le Corre, L., McFadden, L., Sykes, M., Raymond, C., Russell, C.T., 2021. Compositional control on impact crater formation on mid-sized planetary bodies: Dawn at Ceres and Vesta, Cassini at Saturn. Icarus 359, 114343. https://doi.org/10.1016/j.icarus.2021.114343
Scott, D.W., 2012. Multivariate density estimation and visualization, Handbook of Computational Statistics: Concepts and Methods: Second Edition. John Wiley & Sons. https://doi.org/10.1007/978-3-642-21551-3__19
Shoemaker, E.M., 1970. Origin of fragmental debris on the lunar surface and the history of bombardment of the Moon. Inst. Investig. Geol. la Diput. Prov. XXV 24, 27–56.
Smith, P.H., Tamppari, L.K., Arvidson, R.E., Bass, D., Blaney, D., Boynton, W. V., Carswell, A., Catling, D.C., Clark, B.C., Duck, T., DeJong, E., Fisher, D., Goetz, W., Gunnlaugsson, H.P., Hecht, M.H., Hipkin, V., Hoffman, J., Hviid, S.F., Keller, H.U., Kounaves, S.P., Lange, C.F., Lemmon, M.T., Madsen, M.B., Markiewicz, W.J., Marshall, J., McKay, C.P., Mellon, M.T., Ming, D.W., Morris, R. V., Pike, W.T., Renno, N., Staufer, U., Stoker, C., Taylor, P., Whiteway, J.A., Zent, A.P., 2009. H 2 O at the Phoenix Landing Site. Science (80-.). 325, 58–61. https://doi.org/10.1126/science.1172339
Stepinski, T.F., Collier, M.L., 2003. Drainage densities of computationally extracted Martian drainage basins, in: Sixth International Conference on Mars.
Stepinski, T.F., Mendenhall, M.P., Bue, B.D., 2009. Machine cataloging of impact craters on Mars. Icarus 203, 77–87. https://doi.org/10.1016/j.icarus.2009.04.026
Stöffler, D., Ryder, G., 2001. Stratigraphy and isotope ages of lunar geologic units: Chronological standard for the inner solar system. Space Sci. Rev. 96, 9–54. https://doi.org/10.1023/A:1011937020193
Tanaka, K.L., Skinner, J.A., J., Dohm, J.M., Irwin, R.P., Kolb, E.J., Fortezzo, C.M., Platz, T., Michael, G.G., Hare, T.M., 2014. Geologic map of Mars. USGS.

https://doi.org/https://dx.doi.org/10.3133/sim3292

Tanaka, K.L., Skinner, J.A., Hare, T.M., 2005. Geologic Map of the Northern Plains of Mars. U.S. Geol. Surv. Geol. Investig. SIM 2888, 80225.

Warner, N., Gupta, S., Lin, S.Y., Kim, J.R., Muller, J.P., Morley, J.G., 2010. Late Noachian to Hesperian climate change on Mars: Evidence of episodic warming from transient crater lakes near ares vallis. J. Geophys. Res. Planets 115. https://doi.org/10.1029/2009JE003522

Watters, W.A., Geiger, L.M., Fendrock, M., Gibson, R., 2015. Morphometry of small recent impact craters on Mars: Size and terrain dependence, short-term modification. J. Geophys. Res. Planets 120, 226–254. https://doi.org/10.1002/2014JE004630

Werner, S.C., 2009. The global martian volcanic evolutionary history. Icarus 201, 44–68. https://doi.org/10.1016/j.icarus.2008.12.019

Wood, C.A., Andersson, L., 1978. New Morphometric Data for Fresh Lunar Craters. Lunar Planet. Sci. Conf. 9, 16–91.

Young, J., 1940. A Statistical Investigation of Diameter and Distribution of Lunar Craters. J. Br. Astron. Assoc. 50, 309–326.